J. Phys. Chem. C, **2018**, *122*, 1367–1375

DOI: 10.1021/acs.jpcc.7b10277

Manganese(II) molecular sources for plasma-assisted CVD of Mn oxides and fluorides: from precursors to growth process

Davide Barreca,[‡] Giorgio Carraro,[†] Ettore Fois,[§] Alberto Gasparotto,[†] Filippo Gri,[†] Roberta Seraglia,[‡] Martin Wilken,[#] Alfonso Venzo,[‡] Anjana Devi,[#] Gloria Tabacchi[§] and Chiara Maccato[†]***

[‡] CNR-ICMATE and INSTM, Department of Chemical Sciences, Padova University, 35131 Padova, Italy.

[†] Department of Chemical Sciences, Padova University and INSTM, 35131 Padova, Italy.

[§] Department of Science and High Technology, University of Insubria and INSTM, 22100 Como, Italy.

[#] Inorganic Materials Chemistry, Faculty of Chemistry and Biochemistry, Ruhr-University Bochum, 44801 Bochum, Germany.

J. Phys. Chem. C, **2018**, *122*, 1367–1375

DOI: 10.1021/acs.jpcc.7b10277

ABSTRACT

$Mn(dik)_2$•TMEDA complexes [TMEDA = *N*,*N*,*N'*,*N'*-tetramethylethylenediamine; Hdik = 1,1,1,5,5,5-hexafluoro-2,4-pentanedione (Hhfa), or 1,1,1-trifluoro-2,4-pentanedione (Htfa)] are investigated as potential manganese molecular precursors for plasma assisted-chemical vapor deposition (PA-CVD) of Mn-containing nanomaterials. In this regard, the chemico-physical properties, spin states and fragmentation behavior of $Mn(dik)_2$•TMEDA are presented and discussed in the framework of a comprehensive experimental–theoretical investigation. Preliminary PA-CVD validation shows the possibility of varying Mn oxidation state, as well as the system chemical composition from MnF_2 to MnO_2, by simple modulations of the reaction atmosphere, paving the way to a successful utilization of the target compounds in the growth of manganese-containing nanomaterials for different technological applications.

KEYWORDS: Mn precursors; plasma-assisted CVD; MnO_2; MnF_2; nanomaterials.

J. Phys. Chem. C, **2018**, *122*, 1367–1375

DOI: 10.1021/acs.jpcc.7b10277

INTRODUCTION

Manganese-based fluorides and oxides span a wide range of applications, encompassing catalysis, sensing, charge storage and magnetoresistance, among others.[1-5] Many of these applications exploit the multi-valence character and the spin states of Mn, as well as the various stoichiometries and crystal structures of the resulting materials.[6] In particular, MnF_2 thin films and nanostructures have attracted attention for their antiferromagnetic properties,[7-9] as well as anodes for rechargeable lithium batteries[10-12] and electrodes for super/pseudocapacitors.[13] In this regard, efforts have also been dedicated to the production of MnO_2-based systems, which were reported to exhibit high power density and long-term cycling stability.[6,14-15] MnO_2-based nanomaterials have also been the subject of attention in the fabrication of heterogeneous catalysts for a variety of reactions.[4-5,16]

Among the different synthetic routes to manganese-based nanosystems,[6,17] chemical vapor deposition (CVD) and atomic layer deposition (ALD) hold a significant promise for the tailored fabrication of high quality films and nanoarchitectures.[1,18-20] Nevertheless, the successful development of CVD/ALD synthetic protocols is directly dependent on the availability of volatile precursors, ensuring a reproducible mass supply and endowed with clean decomposition/fragmentation patterns.[21-22] So far, only a few reports on the preparation of MnF_2 layers by ALD[23] and CVD[8] are present in the literature, whereas most studies have been dedicated to the synthesis of supported Mn oxide systems. In this context, several molecular precursors have been proposed and tested, encompassing different manganese *bis*(amidinates),[18,24] *bis*(ethylcyclopentadienyl)manganese[1,23,25-29] and various β-diketonates, as, for instance, $Mn(dpm)_3$ (Hdpm = 2,2,6,6-tetramethyl-3,5-heptanedione),[2-3,30] $Mn(acac)_2(H_2O)_2$ (Hacac = 2,4-pentanedione),[20] and $Mn(hfa)_2(H_2O)_2$.[31] Some of these works have reported on the

J. Phys. Chem. C, **2018**, *122*, 1367–1375

DOI: 10.1021/acs.jpcc.7b10277

formation of Mn(II),[29] Mn(III) oxides,[2] Mn_5O_8,[1] as well as Mn_3O_4[3,32] and MnO_2.[3] In most of these studies, the authors report on the formation of unspecified MnO_x systems.[24-26,28] As regards MnF_2, the interrelations between processing conditions and nanomaterial properties have been only scarcely explored so far, and undoubtedly deserve further investigation.

In the framework of CVD approaches, plasma assisted-CVD offers unique advantages for the possibility of controlling precursor reactivity and nano-organization of the resulting material under non-equilibrium conditions.[33-34] In fact, the unique activation exerted by cold plasmas enables the obtainment of crystalline nanodeposits even at low temperatures on thermally labile substrates, with relevant technological advantages.[35] Nevertheless, to the best of our knowledge, only one work from (methylcyclopentadienlyl)manganese tricarbonyl on the PA-CVD of Mn oxide films is available in the literature.[36] The same precursor has also been activated by electronic bombardment to yield Mn-based systems.[21] Even in these cases, the controlled formation of phase-pure manganese oxides with prescribed oxidation states remains a challenging issue,[5,20,27] whose solution requires a proper selection of both molecular precursors and processing conditions. In fact, the possibility of producing manganese-containing systems with controlled oxidation states, phase composition and morphology is a key requirement to tailor their functional behavior for a variety of technological applications.[36]

In this context, the present work proposes the use of Mn(II) diamine diketonates as novel molecular precursors for the PA-CVD of Mn fluoride and oxide nanomaterials. The attention is focused on molecules of general formula $Mn(dik)_2$•TMEDA [TMEDA = *N*,*N*,*N'*,*N'*-tetramethylethylenediamine; Hdik = 1,1,1,5,5,5-hexafluoro-2,4-pentanedione (Hhfa), or 1,1,1-trifluoro-2,4-pentanedione (Htfa)]. Very recently, our group has reported the characterization of the structural and thermal decomposition properties of these compounds, and their successful

J. Phys. Chem. C, **2018**, *122*, 1367–1375
DOI: 10.1021/acs.jpcc.7b10277

validation in preliminary thermal CVD experiments enabling the production of high purity, single-phase Mn_3O_4 nanosystems on different substrates.[37] Encouraged by these results, herein we focus ou attention on the investigation of $Mn(dik)_2$•TMEDA properties in view of their application as PA-CVD precursors. The importance of this study is highlighted by the fact that whereas Mn(II) β-diketonates with unfluorinated ligands are normally converted into Mn(III) β-diketonates,[32] the +2 valence state for manganese can be stabilized by the use of fluorinated β-diketonates,[31] yielding complexes characterized by a monomeric structure and a clean decomposition pattern.[19,38-39] These features are of great importance for PA-CVD applications, for which the number of available precursors is even more restricted than in thermal processes.[33] In this study, $Mn(hfa)_2$•TMEDA and $Mn(tfa)_2$•TMEDA have been investigated in detail by a joint theoretical and experimental multi-technique approach, in order to attain a deep insight into their molecular properties and fragmentation pathways, which are of specific relevance for their ultimate PA-CVD applications. Finally, as a proof of concept, preliminary results obtained through PA-CVD experiments starting from $Mn(tfa)_2$•TMEDA, a completely new PA-CVD precursor, are presented and discussed. The results show that variations of the adopted plasma feeding gases, with particular regard to the presence of oxygen, enable to obtain either MnF_2 or MnO_2 nanodeposits with finely tuned structure, morphology and chemical composition.

EXPERIMENTAL SECTION

$Mn(dik)_2$•TMEDA synthesis and characterization

The preparation of the target compounds carried out following a recently reported synthetic procedure.[37] The compound melting points (m.p.) were measured in air at atmospheric pressure using a FALC melting point device, yielding m.p. = 86°C for $Mn(hfa)_2$•TMEDA[40] and 99°C for

J. Phys. Chem. C, **2018**, *122*, 1367–1375

DOI: 10.1021/acs.jpcc.7b10277

$Mn(tfa)_2$•TMEDA, respectively. Elemental analyses were performed by means of a Fisons Carlo Erba EA1108 apparatus (CHNS version). Calcd. for $Mn(hfa)_2$•TMEDA: C, 32.8%; H, 3.1%; N, 4.8%. Found: C, 33.6%; H, 2.9%; N, 4.8%. Calcd. for $Mn(tfa)_2$•TMEDA: C, 40.3%; H, 5.1%; N, 5.9%. Found: C, 40.9%; H, 5.1%; N, 6.0%.

Density functional theory (DFT) geometry optimizations (GO) on $Mn(dik)_2$•TMEDA complexes and molecular ions were performed using the Gaussian 09[41] code. The thermal behaviour of such species was explored by first principles molecular dynamics simulations (FPMD)[42] using the CPMD code[43] and a computational setup adopted for other $M(hfa)_2$•TMEDA systems (M = Cu,[44-45] Zn,[46] and Fe[47]), enhanced with dispersion corrections.[48] Technical details of all GO and FPMD calculations are reported in the Computational Section in the SI.

^1H and ^{13}C nuclear magnetic resonance (NMR) spectra were obtained at 25°C on 0.1 M solutions of the compounds in $CDCl_3$ using a Bruker AC-200 MNR spectrometer, equipped with a 4.7 T crio-magnet and operating at ν_o = 200.13 MHz on ^1H and ν_o = 50.32 MHz on ^{13}C. Chemical shift values (δ, ppm) were reported with reference to internal Me_4Si. For ^1H spectra, the largest allowed sweep width of 74 kHz (≈370 ppm) was used. In the case of ^{13}C measurement, spectra were first recorded using 0.0 ppm as offset using the largest possible sweep width (≈700 ppm). The offset was then shifted downfield and upfield by 700 ppm steps to cover all the possible resonance regions, until the disappearance of resonances. A scan number of at least 4 millions was used in each experiments (time domain = 4K Words, repetition time = 0.2 s). Only very broad lines were observed in the ^{13}C spectra, the half-width ($hw_{1/2}$) being typically 30 KHz (70 kHz for resonances at δ ≈230-260).

Infrared (IR) spectra were recorded in transmittance mode on KBr pellets of the target compounds by using a Thermo-Nicolet Nexus 860 instrument (peak resolution = 4 cm^{-1}).

J. Phys. Chem. C, **2018**, *122*, 1367–1375

DOI: 10.1021/acs.jpcc.7b10277

Theoretical vibrational frequencies were compared with experimental IR data. Calculated minima had all positive frequencies and were in the high-spin state (see Computational Section, SI).

Electron impact-mass spectrometry (EI-MS) spectra were recorded by using a Varian MAT spectrometer adopting standard EI conditions (E_I = 70 eV).

PA-CVD of Mn-containing nanosystems

MnF_2 and MnO_2 nanosystems were deposited by means of a custom-built two-electrode PA-CVD reactor [radio frequency (RF) =13.56 MHz; electrode diameter = 9 cm; electrode-to-electrode distance = 6 cm].[49] Before deposition, Si(100) substrates (2×2 cm^2) were ultrasonically cleaned in a sulphonic detergent solution, rinsed with deionized water and then with isopropylic alcohol. After drying in air, they were mounted by means of metallic clips on the reactor grounded electrode, whose temperature was maintained at 300°C. Experiments were performed for 1 h at a total pressure of 1.0 mbar and a RF-power of 20 W. The precursor (0.20 g for each deposition), placed in an external glass reservoir, was vaporized at 85°C by means of an oil bath, and transported into the reaction chamber by an Ar flow [60 standard cubic centimeters per minute (sccm)]. To prevent detrimental condensation processes, gas lines connecting the precursor vessel and the reactor were maintained at 150°C by means of external heating tapes throughout each deposition. For MnF_2 and MnO_2 growth, additional Ar (15 sccm) and Ar+O_2 (15+15 sccm) flows, respectively, were introduced directly into the reactor chamber using separated inlets.

Material characterization

The system crystallinity was investigated by X-ray diffraction (XRD) analyses using a Bruker D8 Advance diffractometer, using a CuKα source (λ = 1.5418 Å) powered at 40 kV, 40 mA, at a

J. Phys. Chem. C, **2018**, *122*, 1367–1375
DOI: 10.1021/acs.jpcc.7b10277

fixed incidence angle of 1.0°. The average crystallite sizes were estimated by using the Scherrer formula.

The nanomaterial morphology was analyzed by field emission-scanning electron microscopy (FE-SEM) using a Zeiss SUPRA 40VP instrument, operated at a primary beam voltage of 10 kV. X-ray photoelectron spectroscopy (XPS) analyses were carried out with a Perkin–Elmer Φ 5600ci spectrometer using a standard AlKα source (excitation energy = 1486.6 eV). Binding energy (BE; standard deviation = ±0.2 eV) charging shifts were corrected by assigning to the adventitious C1s signal a position of 284.8 eV.[50] After background subtraction, spectra were fitted, where necessary, with Gaussian–Lorentzian functions. Atomic percentages were evaluated using Φ V5.4A sensitivity factors. Ar^+ sputtering was carried out at 4.0 kV, with an Ar partial pressure of 5×10^{-8} mbar.

RESULTS AND DISCUSSION

We begin by taking into account the main structural features of both $Mn(hfa)_2$•TMEDA and $Mn(tfa)_2$•TMEDA compounds (Figure 1). As can be observed, irrespective of the used β-diketonate, the coordination environment around the Mn(II) center is a distorted octahedron, as already reported for homologous $M(hfa)_2$•TMEDA complexes where M = Fe,[51] Co,[19] Cu[38] and Zn.[46] As regards $Mn(tfa)_2$•TMEDA, three structural isomers, characterized by different relative positioning of the $–CH_3$ and $–CF_3$ groups, would be, in principle, possible (see Figure 1). Calculations were thus performed on all three isomers to understand why only one of them – namely, iso1 – was actually found in the crystallized compound.[37] In line with the experimentally determined structure, the most stable isomer, iso1 [see Table S1, Supporting Information (SI)],

J. Phys. Chem. C, **2018**, *122*, 1367–1375

DOI: 10.1021/acs.jpcc.7b10277

provided the closest agreement with the experimental IR spectrum (Figure S1, SI). By comparing the geometries of the three isomers, the greater stability of iso1 was attributed to the co-presence of both methyl groups, which have a lower steric hindrance than $-CF_3$ ones, in the octahedral basal plane.

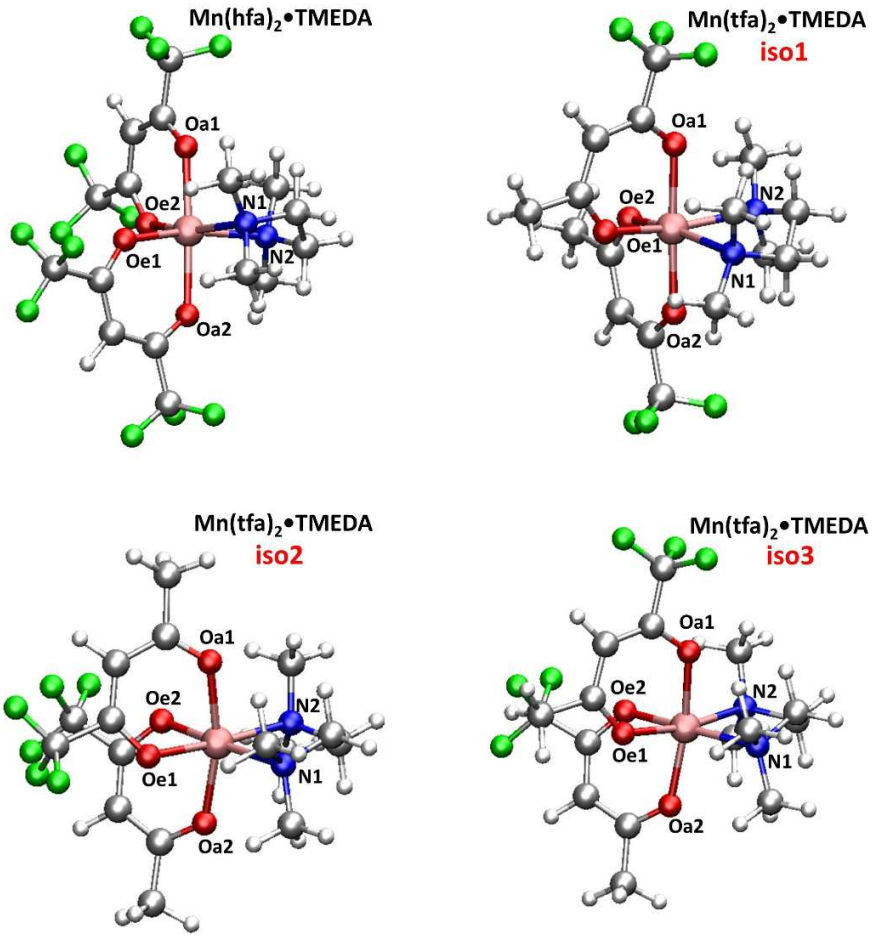

Figure 1. Calculated structures of $Mn(hfa)_2$•TMEDA and $Mn(tfa)_2$•TMEDA. For the latter compound, the three possible isomers (iso1, iso2, and iso3) are shown. The two equatorial oxygens, which lie in the octahedral basal plane, trans to the TMEDA ligand, are labelled as Oe (Oe1, Oe2). The two axial oxygens, positioned at the vertices of the coordination octahedron, are labelled as Oa (Oa1, Oa2). Calculated energy differences (ΔE) between the three optimized geometries predict that the most stable isomer for $Mn(tfa)_2$•TMEDA is iso1 [ΔE (iso2-iso1) = 2.9 kcal×mol^{-1}; ΔE (iso3-iso1) = 2.4 kcal×mol^{-1}]. Atom color codes: Mn, pink; O, red; F, green; N,

J. Phys. Chem. C, **2018**, *122*, 1367–1375
DOI: 10.1021/acs.jpcc.7b10277

blue; C, grey; H, white.

Beside obvious differences in the diketonate ligands, the structures of the two compounds share many important features, especially in the Mn coordination environment. Their geometrical parameters, closely related to the strength of the metal-ligand interactions, yield preliminary indications on possible decomposition routes of the complexes.[45-46] Importantly, in both precursors the Mn–N distances are longer than the Mn–O ones, as observed for M(hfa)$_2$•TMEDA (M = Fe,[51] Co,[19] and Zn[46]). This feature, which may suggest a looser binding of TMEDA to the metal center,[47] is more for Mn(tfa)$_2$•TMEDA, in which the Mn–N and Mn–O coordination distances differ almost by 0.2 Å (Table 1).

For both complexes, the sextet spin state was found to be the most stable (see Computational section, SI), evidencing thus the paramagnetic character of both molecular systems. Owing to the latter feature, NMR analyses on Mn(dik)$_2$•TMEDA are indeed quite challenging and, in fact, no previous studies reporting such characterization on similar systems are available in the literature. Following our recent works on high-spin molecular systems, such as Fe(hfa)$_2$•TMEDA[39] and Fe(dpm)$_3$,[33] in this paper NMR characterization has been extended to the present Mn precursors. As a matter of fact, the obtained chemical shift values, as well as the line broadening for the obtained compounds, are strongly affected by their intense paramagnetism, the signals being dramatically shifted downfield or upfield by the coupling of the ^{1}H nuclear spin with the unpaired electron(s) density. The ^{1}H-NMR spectrum of Mn(hfa)$_2$•TMEDA (Figure S2, SI) consisted mainly of a broad resonance at δ 2.0 ($hw_{1/2}$ ≈ 1.3 KHz) with three superimposed less broadened resonances at δ 1.26 and δ 0.1 ($hw_{1/2}$ ≈ 40 Hz). The same signal was observed in the ^{1}H-NMR spectrum of Mn(tfa)$_2$•TMEDA, with one additional broad resonance located at δ 49 ($hw_{1/2}$ ≈ 4 KHz) attributed to protons of the methyl groups bonded to carbonyls, that were absent

J. Phys. Chem. C, **2018**, *122*, 1367–1375

DOI: 10.1021/acs.jpcc.7b10277

in the former compound. No other signals were detected outside the interval of chemical shift values ranging from 183 δ to -183 δ. ^{13}C-NMR spectra (not shown) displayed a series of extremely broadened resonances in the chemical shift range 750 δ to -750 δ. The $hw_{1/2}$ values were ≈ 30 kHz, except for the broad resonance at δ = 245±15 ($hw_{1/2}$ value ≈ 70 kHz), which was attributed to the carbon nuclei nearest to the Mn center, *i.e.*, those belonging to carbonyl groups.

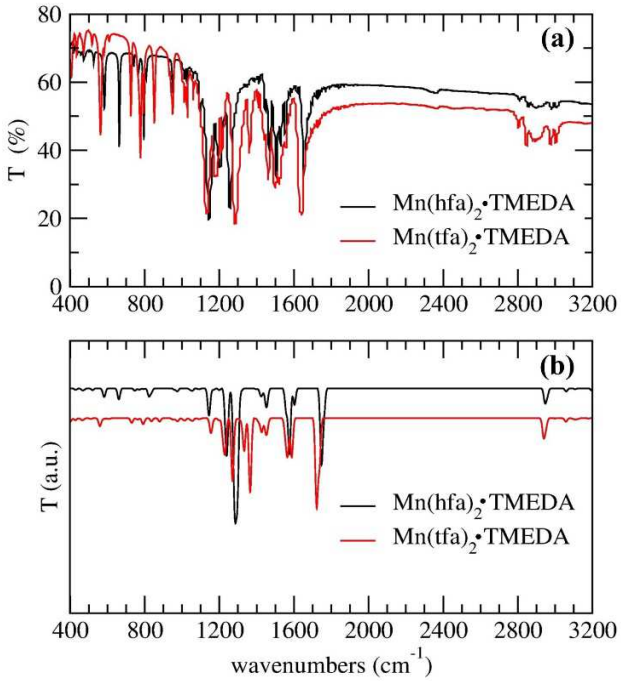

Figure 2. Comparison of experimental (a) and simulated (b) IR spectra of $Mn(hfa)_2$•TMEDA and $Mn(tfa)_2$•TMEDA.

The experimental and simulated IR spectra of the two Mn complexes (Figure 2) were in line with those previously reported for $M(hfa)_2$•TMEDA (with M = Fe, Cu).[38,51] Due to the different nature of the used dik ligands, the main differences between the spectra of the two compounds (compare Table S2, SI) were found in the 1200–1400 cm^{-1} range - mainly pertaining to $–CF_3$ and $–CH_3$ vibrations - and in the carbonyl stretching region (Figure 2). In particular, the peak at 1360 cm^{-1}, which appeared only in the $Mn(tfa)_2$•TMEDA spectrum, is specific of the $–CH_3$ bending

J. Phys. Chem. C, **2018**, *122*, 1367–1375

DOI: 10.1021/acs.jpcc.7b10277

modes. The carbonyl peak (found at 1656 and 1640 cm^{-1} for $Mn(hfa)_2$•TMEDA and $Mn(tfa)_2$•TMEDA, respectively) was more red-shifted for the complex with the shorter Mn–O distances, i.e. $Mn(tfa)_2$•TMEDA (Table 1), indicating that tfa is bound to Mn more tightly than hfa. For both complexes, Mn–O stretching frequencies were higher than Mn–N ones, and the effect was more pronounced for $Mn(tfa)_2$•TMEDA. This result indicated that, in the minimum structures obtained from GO (i.e. at 0 K), the diketonate is bound to Mn more strongly than the diamine, especially in the case of tfa. To verify if this bonding scheme holds also under standard conditions, FPMD simulations were performed. Both complexes were stable at room temperature, exhibiting, nonetheless, significant thermal oscillations of bond distances with respect to the average values (Table 1). Irrespective of the β-diketonate nature, the average metal-ligand coordination distances (slightly higher than the optimized geometry values, Table 1) confirmed the greater lability of Mn–N bonds with respect to Mn–O ones, in line with previous results on $Fe(hfa)_2$•TMEDA.[37, 38, 53]

	$Mn(hfa)_2$•TMEDA		**$Mn(tfa)_2$•TMEDA**		**$Mn(hfa)_2$•TMEDA$]^{+\bullet}$**		**$[Mn(tfa)_2$•TMEDA$]^{+\bullet}$**	
Bond[c]	GO	FPMD	GO	FPMD	GO	FPMD	GO	FPMD
Mn-N1	**2.248**	**2.36±0.12**	**2.303**	**2.39±0.14**	2.036	2.14±0.04	2.099	**2.25±0.10**
Mn-N2	**2.248**	**2.34±0.09**	**2.303**	**2.39±0.14**	2.036	2.14±0.04	**2.253**	**2.25±0.11**
Mn-Oa1	2.123	2.15±0.10	2.117	2.17±0.09	**2.116**	**2.16±0.08**	1.852	1.97±0.14
Mn-Oa2	2.123	2.16±0.10	2.117	2.17±0.11	**2.116**	**2.16±0.09**	1.846	1.99±0.12
Mn-Oe1	2.128	2.17±0.10	2.120	2.15±0.10	1.889	1.95±0.06	1.949	2.05±0.12

Table 1. $Mn(dik)_2$•TMEDA and $[Mn(dik)_2$•TMEDA$]^{+\bullet}$ coordination bond lengths from GO (Å) and average values <r> ± Δr (Å) from FPMD simulations (25°C). Δr indicates the average amplitude of thermal oscillations of the metal-ligand bond distances.[45] Values in bold refer to the longest metal-ligand bonds. Spin multiplicity: sextet, for $Mn(hfa)_2$•TMEDA and $Mn(tfa)_2$•TMEDA; quintet, for $[Mn(hfa)_2$•TMEDA$]^{+\bullet}$ and $[Mn(tfa)_2$•TMEDA$]^{+\bullet}$.

J. Phys. Chem. C, **2018**, *122*, 1367–1375

DOI: 10.1021/acs.jpcc.7b10277

Taken together, these results highlighted a significant structural flexibility of the complexes under standard conditions, particularly evident for the Mn–N bonds. In this regard, previous studies on $M(hfa)_2$•TMEDA precursors showed that the typical thermal CVD conditions significantly affect the most labile metal-ligand bonds,[38,44-47] whose identification might provide insights into precursor decomposition mechanisms. In the present case, the most labile bonds of both complexes are clearly the Mn–N ones, which would suggest an easier loss of TMEDA irrespective of the nature of the dik ligand. Nevertheless, it is worth recalling that PA-CVD conditions significantly differ from thermal-CVD ones, since the use of cold plasmas directly induces precursor ionization.

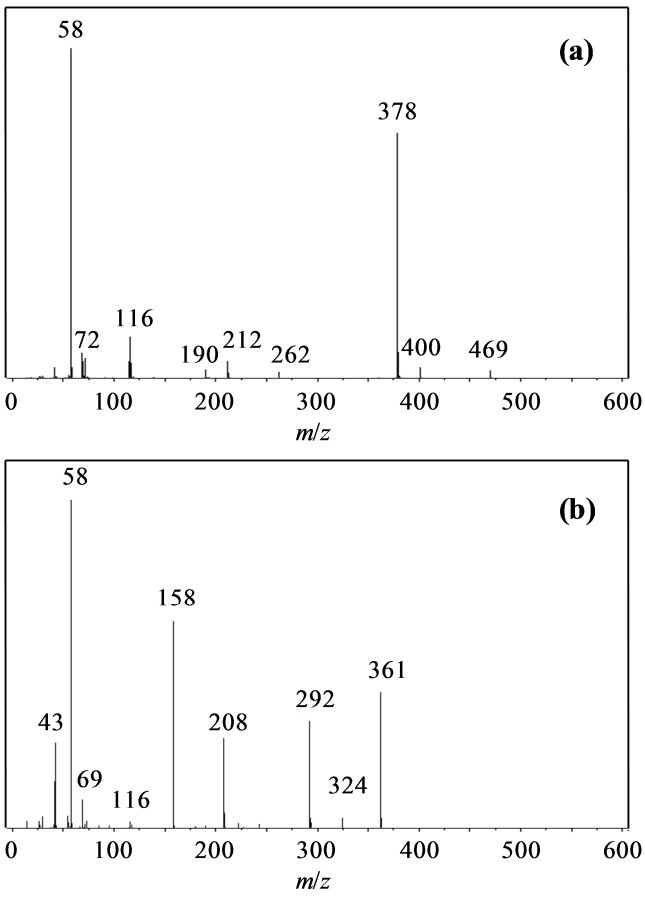

Figure 3. EI-MS spectra of: (a) $Mn(hfa)_2$•TMEDA; (b) $Mn(tfa)_2$•TMEDA.

J. Phys. Chem. C, **2018**, *122*, 1367–1375

DOI: 10.1021/acs.jpcc.7b10277

In order to shed further light on the target compound fragmentation and gain useful information for their possible use as PA-CVD precursors, EI-MS studies were carried out (Figure 3). For both compounds, the base peak of the spectra, located at *m*/*z* = 58, corresponded to $(CH_3)_2NCH_2^+$ ionic species originating from TMEDA cleavage. No molecular ion signals and, in general, no peaks at high *m*/*z* values were detected,[51] suggesting the absence of polynuclear aggregates. This conclusion, in line with the results obtained by the other analysis techniques, is of importance for the application of Mn(dik)$_2$•TMEDA as PA-CVD precursors, since the presence of oligomeric structures would negatively affect both precursor mass transport properties and decomposition pathways.

A careful examination of the obtained results evidenced a different behaviour of the two complexes under EI conditions. In fact, even if peaks due to losses of dik and TMEDA are well detected for both complexes, the relative intensities for these fragments are substantially different, as summarized in Table S3, SI. Even if for both complexes the base peak is due to $(CH_3)_2NCH_2^+$ species (m/z 58), in the case of Mn(hfa)$_2$•TMEDA, the loss of hfa leads to the ion at *m*/*z* = 378 (relative abundance = 74%), while the loss of TMEDA yields the ionic species at *m*/*z* = 469 (2%). In contrast, for Mn(tfa)$_2$•TMEDA, the diamine loss, generating the ion at *m*/*z* = 361 (42%), is favored with respect to tfa release (ion at *m*/*z* = 324, 4%). Other low abundance peaks are due to losses of CF_2/CF_3 moieties from L-containing fragments, leading to radical cations, as previously observed for similar compounds, such as Fe(hfa)$_2$•TMEDA[51] and Co(hfa)$_2$•TMEDA.[52] It remains to understand, however, why the loss of dik, or TMEDA, ligands is predominant for dik = hfa or tfa, respectively, in spite of the similarities in the structure and room-temperature behaviour of the two complexes. To address this issue, we calculated the minimum energy structures of putative $[Mn(dik)_2•TMEDA]^{+•}$ radical cations that might be

J. Phys. Chem. C, **2018**, *122*, 1367–1375
DOI: 10.1021/acs.jpcc.7b10277

initially formed in EI-MS experiments, as well as in PA-CVD processes. In view of the provided energy inputs, such radical cations might well exhibit different spin multiplicities. Nevertheless, calculations performed for $[Mn(hfa)_2•TMEDA]^{+•}$ and $[Mn(tfa)_2•TMEDA]^{+•}$ by considering all possible spin states (Computational Section and Tables S4-S5, SI) indicated that the quintet spin state is energetically favored over the other ones. Thus, irrespective of the dik ligand nature, ionization should preferentially produce radical cations in the quintet spin state. The energy required to form such species amounts to 173.2 and 158.9 kcal×mol^{-1}, for $Mn(hfa)_2•TMEDA]^{+•}$ and $[Mn(tfa)_2•TMEDA]^{+•}$, respectively. Such values are in line with those recently found for a Fe-containing PA-CVD precursor[33] and fully compatible with the energy-intensive conditions associated to the use of cold plasmas. Interestingly, the ionization energy was lower for $Mn(tfa)_2$•TMEDA, which could possibly make this compound a better candidate as a potential PA-CVD precursor.

As concerns structural properties, data in Table 1 reveal that, irrespective of the β-diketonate, radical cations basically maintain a *pseudo*-octahedral coordination environment, with metal-ligand distances shorter than in the parent complexes. Nevertheless, whereas the latter had very similar geometries (Table 1), the most stable structures of molecular ions are indeed strikingly different (Figure 4). In particular, the longest metal-ligand distances – thus, presumably the most labile bonds – involve the diketonate in $[Mn(hfa)_2•TMEDA]^{+•}$, and the diamine in $[Mn(tfa)_2•TMEDA]^{+•}$ (Table 1). These data would suggest a different fragmentation behavior for the two radical cations: the loss of a hfa moiety should be favored for $[Mn(hfa)_2•TMEDA]^{+•}$, whereas $[Mn(tfa)_2•TMEDA]^{+•}$ should preferentially decompose by releasing TMEDA. To investigate whether such structural differences were maintained even under operative conditions, FPMD of $[Mn(dik)_2•TMEDA]^{+•}$ radical cations were performed at 180°C. Simulations results

J. Phys. Chem. C, **2018**, *122*, 1367–1375

DOI: 10.1021/acs.jpcc.7b10277

(Table 1), basically confirm that TMEDA is less tightly bound than dik in $[Mn(tfa)_2•TMEDA]^{+•}$, whereas the opposite occurs in $[Mn(hfa)_2•TMEDA]^{+•}$, rationalizing thus the different fragmentation patterns evidenced by EI-MS experiments (Figure 3, Table S3, SI). Finally, $Mn(tfa)_2$•TMEDA, the complex with the lower ionization energy, never utilized in PA-CVD processes so far, was chosen for proof-of-concept preliminary experiments aimed at validating its applicability as PA-CVD precursor.

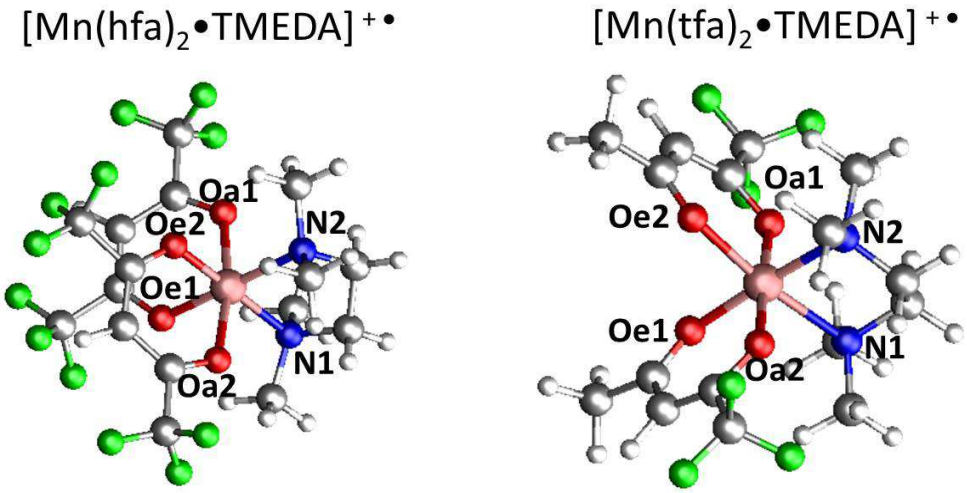

Figure 4. Calculated minimum structures of $[Mn(dik)_2•TMEDA]^{+•}$ radical cations in the quintet spin state. Atom color codes as in Figure 1.

Experiments were carried out at 300°C, a temperature much lower than those reported in previous studies for the thermal CVD growth of Mn fluorides and oxides from $Mn(hfa)_2$•TMEDA.[8,32] For the sample prepared in the absence of oxygen (Figure 5), the XRD pattern exhibited peaks located at 2ϑ = 26.0°, 32.8°, 37.0°, 37.8° and 50.2°, that could be respectively ascribed to the (110), (101), (200), (111) and (211) reflections of tetragonal MnF_2[53] [mean crystallite size = (30±4) nm]. In a different way, the introduction of oxygen in the plasma resulted in the disappearance of fluoride reflections and in the presence of signals at 2ϑ = 28.7°,

J. Phys. Chem. C, **2018**, *122*, 1367–1375

DOI: 10.1021/acs.jpcc.7b10277

37.4° and 42.8°, related to the (110), (101) and (111) planes of tetragonal MnO_2 [*pyrolusite*; mean crystallite size = (20±5) nm].[54]

This result evidences the high oxidizing power of oxygen-containing plasmas, that, in the present case, enable an increase of the manganese oxidation state from +2 to +4 and a switch of the system structure from MnF_2 to MnO_2. A comparison of the obtained relative intensities with those pertaining to the reference patterns enabled to rule out the occurrence of significant preferential orientation phenomena in the case of MnF_2. In a different way, for the MnO_2 specimen, the $I_{(110)}/I_{(101)}$ intensity ratio was reversed with respect to the powder spectrum,[54] suggesting the occurrence of possible preferred orientation effects/anisotropic growth.

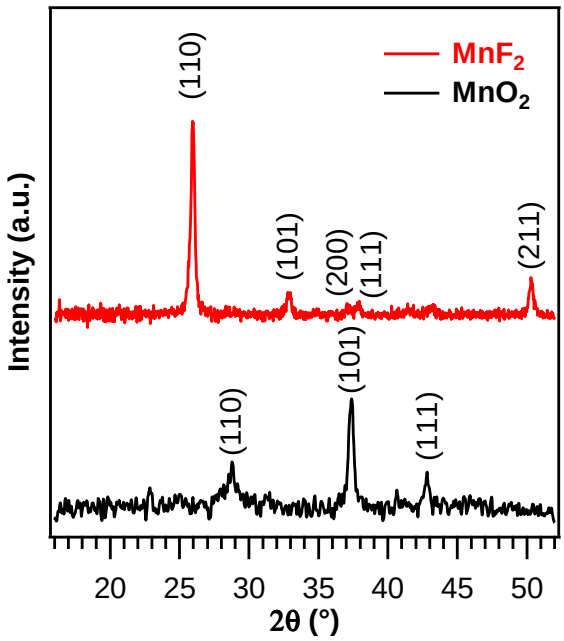

Figure 5. XRD patterns of Mn-containing nanodeposits obtained without (red pattern) and with (black pattern) the introduction of an O_2 flow in the used plasma.

To investigate the system nano-organization as a function of oxygen presence in the reaction environment, both plane-view and cross-sectional FE-SEM analyses were performed (Figure 6).

J. Phys. Chem. C, **2018**, *122*, 1367–1375

DOI: 10.1021/acs.jpcc.7b10277

For MnF_2, the reported micrographs display the formation of a compact and highly faceted deposit, with an average aggregate size of (90±30) nm and a mean thickness of (160±10) nm. In a different way, the MnO_2 specimen was characterized by the presence of an underlayer "seed layer" [average aggregate length and width = (60±10) nm and (16±5) nm, respectively; mean thickness = (300±30) nm] in contact with the substrate surface, on which the growth of randomly distributed protruding nano-leaves (average lateral dimensions = (1.0±0.2) μm; average vertical size = (1.4±0.3) μm] could be observed. Such kind of anisotropic growth, in line with the above presented XRD data, yielded high surface area nanostructures, paving the way to possible catalytic and photocatalytic applications of the developed nanomaterials.

J. Phys. Chem. C, **2018**, *122*, 1367–1375

DOI: 10.1021/acs.jpcc.7b10277

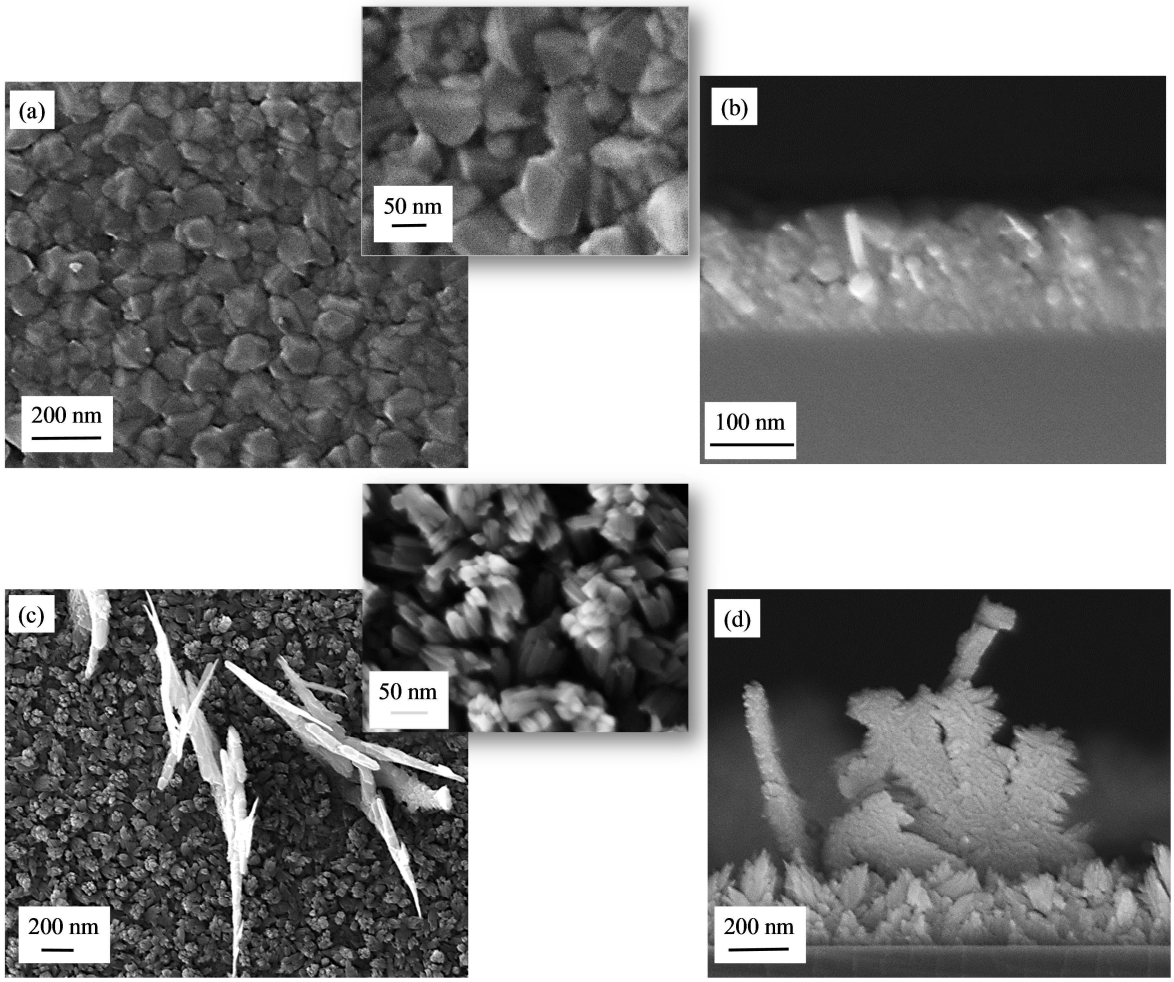

Figure 6. Plane-view (left) and cross-sectional (right) FE-SEM micrographs for MnF_2 (a, b) and MnO_2 (c, d) nanodeposits.

The system chemical composition was finally examined by XPS. To this aim, Figure 7a displays wide-scan XPS spectra of both MnF_2 and MnO_2 nanodeposits, that were dominated by Mn photopeaks. Irrespective of the synthetic conditions, carbon signal disappearance after a few minutes of Ar^+ erosion indicated that it mainly arose from exposure to the external atmosphere, confirming a clean precursor decomposition under the adopted conditions.

J. Phys. Chem. C, **2018**, *122*, 1367–1375

DOI: 10.1021/acs.jpcc.7b10277

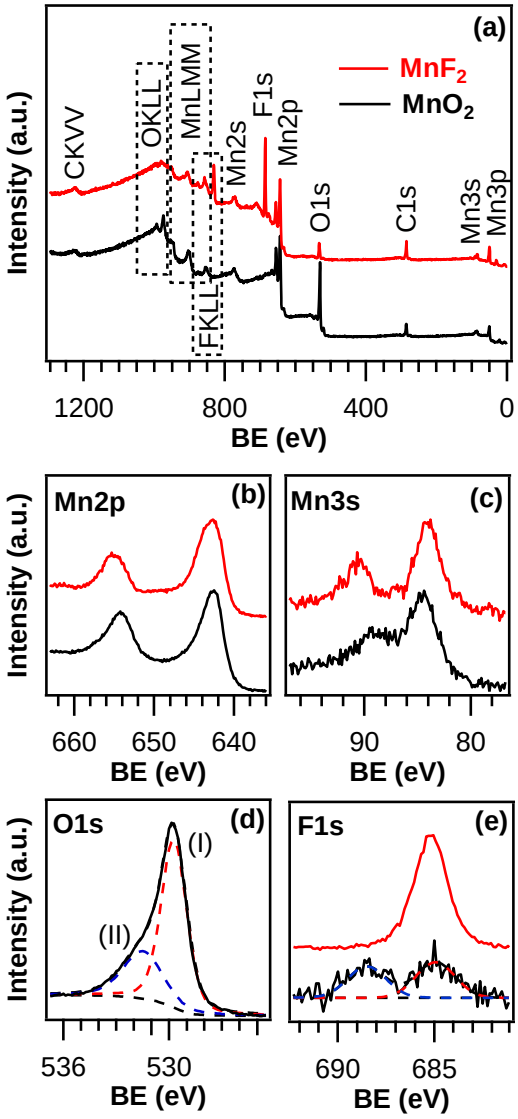

Figure 7. (a) Surface-wide-scan XPS spectra for MnF_2 and MnO_2 specimens. The detailed (b) Mn2p, (c) Mn3s, (d) O1s, and (e) F1s surface photoelectron peaks pertaining to the two samples are also reported.

A similar phenomenon took place also for the O1s signal in the MnF_2 sample, highlighting the obtainment of a pure fluoride phase. These issues are of considerable importance, taking into account that the only previous PA-CVD work on MnO_x fabrication reported on the obtainment of highly contaminated systems.[36]

J. Phys. Chem. C, **2018**, *122*, 1367–1375

DOI: 10.1021/acs.jpcc.7b10277

Quantitative analyses yielded atomic F/Mn and O/Mn ratios of 1.4 and 1.7, for depositions carried out in the absence/presence of oxygen respectively. Such values are both lower than the expected stoichiometric ones, suggesting the presence of an appreciable surface defectivity. This feature could play an important role in determining the reactivity of the obtained materials in various technological fields, ranging from sensing to (photo)catalytic applications.The Mn2p photopeaks for the target materials, displayed in Figure 7b, were in good agreement with literature data for MnF_2 and MnO_2 in terms of both shape and position [for MnF_2, BE($Mn2p_{3/2}$) = 642.7 eV and spin-orbit splitting (SOS) = 12.6 eV;[10,12,55] for MnO_2, BE($Mn2p_{3/2}$) = 642.5 eV and SOS = 11.8 eV, respectively.[5,15-16] The manganese oxidation state in the two cases was further confirmed by examining the magnitude of the Mn3s (Figure 7c) multiplet splitting separation, which is considered as a fingerprint for this parameter.[3] In line with previous studies, the obtained values were 6.2 and 4.7 eV for MnF_2 and MnO_2, respectively.[13,36] For the latter system, the main contribution (I) to the O1s photopeak (Figure 7d) at 529.7 eV was attributed to lattice oxygen in MnO_2, whereas the second minor band (II) located at BE = 531.5 eV could be mainly ascribed to adsorbed –OH groups/chemisorbed oxygen species.[5-6,14,16] For MnF_2, the F1s signal (Figure 7e) was characterized by a single component centred at a BE value of 685.2 eV, in agreement with the occurrence of lattice fluoride.[10,55] Even for the MnO_2 sample, the F1s surface peak, though much less intense than in the previous case, could be detected (atomic F/Mn ratio = 0.04). In this case, two different bands contributed to this photopeak, a high BE one (BE = 688.5 eV), due to CF_x moieties, and a second one at BE = 684.9 eV, traced back to F incorporation into manganese oxide lattice.[10,49,56-57] These results may play a major role for the eventual tailoring of material functional properties in gas sensing and photocatalytic applications, as already observed for iron and cobalt oxides obtained via PA-CVD from $M(hfa)_2$•TMEDA (M = Fe, Co)

J. Phys. Chem. C, **2018**, *122*, 1367–1375

DOI: 10.1021/acs.jpcc.7b10277

precursors.[34,52,58-59]

CONCLUSIONS

In the present work, $Mn(dik)_2$•TMEDA complexes have been characterized for eventual applications as PA-CVD precursors. The detailed characterization of their properties and reactivity, never reported in the literature so far, disclosed the microscopic behavior of their molecular ions and highlighted their potential for the target applications. Both compounds possess a monomeric structure with a pseudo-octahedral Mn core. Their fragmentation pathways, based on the initial loss of the diamine or of the diketonate, depending on the ligand nature, suggest a remarkable versatility of these precursors, which paves the way to their favorable application in PA-CVD processes. In this regard, the utilization of Ar or Ar-O_2 plasmas enabled to drive the precursor conversion into MnF_2 or MnO_2, respectively. The fabricated systems, obtained for the first time by the proposed route, are characterized by well controlled phase composition and manganese oxidation state. These features, along with the tailoring of system defectivity and morphology, are favorable pre-requisites in view of various functional applications, for instance in photocatalysis for pollutant decomposition/hydrogen production and gas sensing of flammable/toxic analytes. In this regard, variations of PA-CVD conditions and tests of $Mn(hfa)_2$•TMEDA in similar processes will be a part of our future studies devoted to the synthesis of MnO_2-based materials.

ASSOCIATED CONTENT

J. Phys. Chem. C, **2018**, *122*, 1367–1375

DOI: 10.1021/acs.jpcc.7b10277

Supporting Information. The Supporting Information is available free of charge on the ACS Publications website. NMR characterization and computational results on $Mn(dik)_2$•TMEDA.

AUTHOR INFORMATION

Corresponding Authors

* gloria.tabacchi@uninsubria.it

** chiara.maccato@unipd.it

ACKNOWLEDGMENTS

Financial support from Padova University ex-60% 2015–2017, P-DiSC #SENSATIONAL BIRD2016-UNIPD projects, and ACTION post-doc fellowship, as well as from Insubria University FAR 2015-2016, is gratefully acknowledged. Thanks are also due to Dr. Lorenzo Bigiani and Mr. Loris Calore (Padova University) for skilful support and elemental microanalyses.

J. Phys. Chem. C, **2018**, *122*, 1367–1375

DOI: 10.1021/acs.jpcc.7b10277

REFERENCES

(1) Young, M. J.; Hare, C. D.; Cavanagh, A. S.; Musgrave, C. B.; George, S. M. Rapid Growth of Crystalline Mn_5O_8 by Self-Limited Multilayer Deposition using $Mn(EtCp)_2$ and O_3. *ACS Appl. Mater. Interfaces* **2016**, *8*, 18560-18569.

(2) Nakamura, T.; Tai, R.; Nishimura, T.; Tachibana, K. Spectroscopic Study on Metallorganic Chemical Vapor Deposition of Manganese Oxide Films. *J. Electrochem. Soc.* **2005**, *152*, C584-C587.

(3) Nilsen, O.; Fjellvåg, H.; Kjekshus, A. Growth of Manganese Oxide Thin Films by Atomic Layer Deposition. *Thin Solid Films* **2003**, *444*, 44-51.

(4) Yang, M.; Kim, D. S.; Sim, J.-W.; Jeong, J.-M.; Kim, D. H.; Choi, J. H.; Kim, J.; Kim, S.-S.; Choi, B. G. Synthesis of Vertical MnO_2 Wire Arrays on Hemp-Derived Carbon for Efficient and Robust Green Catalysts. *Appl. Surf. Sci.* **2017**, *407*, 540-545.

(5) Luo, S.; Zhou, W.; Xie, A.; Wu, F.; Yao, C.; Li, X.; Zuo, S.; Liu, T. Effect of MnO_2 Polymorphs Structure on the Selective Catalytic Reduction of NO_x with NH_3 over TiO_2–Palygorskite. *Chem. Eng. J.* **2016**, *286*, 291-299.

(6) Singu, B. S.; Yoon, K. R. Porous Manganese Oxide Nanospheres for Pseudocapacitor Applications. *J. Alloys Compd.* **2017**, *695*, 771-778.

(7) Zhao, Y.; Fu, S. F.; Li, H.; Wang, X. Z. Bistable Transmission of Antiferromagnetic Fabry-Perot Resonator. *J. Appl. Phys.* **2011**, *110*, 023512.

(8) Malandrino, G.; Toro, R. G.; Catalano, M. R.; Fragalà, M. E.; Rossi, P.; Paoli, P. Pompon-Like MnF_2 Nanostructures from a Single-Source Precursor through Atmospheric Pressure Chemical Vapor Deposition. *Eur. J. Inorg. Chem.* **2012**, *2012*, 1021-1024.

(9) Veerakumar, V.; Camley, R. E. Magnetostatic Bulk and Surface Spin-Wave Focusing in Antiferromagnetic Thin Films. *Phys. Rev. B* **2010**, *81*, 174432.

(10) Rui, K.; Wen, Z.; Lu, Y.; Jin, J.; Shen, C. One-Step Solvothermal Synthesis of Nanostructured Manganese Fluoride as an Anode for Rechargeable Lithium-Ion Batteries and Insights into the Conversion Mechanism. *Adv. Energy Mater.* **2015**, *5*, 1401716.

(11) Rui, K.; Wen, Z.; Huang, X.; Lu, Y.; Jin, J.; Shen, C. High-performance Lithium Storage in an Ultrafine Manganese Fluoride Nanorod Anode with Enhanced Electrochemical Activation Based on Conversion Reaction. *Phys. Chem. Chem. Phys.* **2016**, *18*, 3780-3787.

(12) Rui, K.; Wen, Z.; Lu, Y.; Shen, C.; Jin, J. Anchoring Nanostructured Manganese Fluoride on Few-Layer Graphene Nanosheets as Anode for Enhanced Lithium Storage. *ACS Appl. Mater. Interfaces* **2016**, *8*, 1819-1826.

(13) Ma, R.; Zhou, Y.; Yao, L.; Liu, G.; Zhou, Z.; Lee, J.-M.; Wang, J.; Liu, Q. Capacitive Behaviour of MnF_2 and CoF_2 Submicro/Nanoparticles Synthesized via a Mild Ionic Liquid-Assisted Route. *J. Power Sources* **2016**, *303*, 49-56.

(14) Wu, Z.-S.; Ren, W.; Wang, D.-W.; Li, F.; Liu, B.; Cheng, H.-M. High-Energy MnO_2 Nanowire/Graphene and Graphene Asymmetric Electrochemical Capacitors. *ACS Nano* **2010**, *4*, 5835-5842.

(15) Cakici, M.; Kakarla, R. R.; Alonso-Marroquin, F. Advanced Electrochemical Energy Storage Supercapacitors Based on the Flexible Carbon Fiber Fabric-Coated with Uniform Coral-Like MnO_2 Structured Electrodes. *Chem. Eng. J.* **2017**, *309*, 151-158.

(16) Li, J.; Qu, Z.; Qin, Y.; Wang, H. Effect of MnO_2 Morphology on the Catalytic Oxidation of Toluene over Ag/MnO_2 Catalysts. *Appl. Surf. Sci.* **2016**, *385*, 234-240.

(17) Kyutt, R. N.; Banshchikov, A. G.; Kaveev, A. K.; Sokolov, N. S.; Lomov, A. A.; Ohtake, Y.; Tabuchi, M.; Takeda, Y. Structure and Surface Morphology of MnF_2 Epitaxial Layers Grown on Grooved and Ridged CaF_2 (110) Surface. *J. Phys. D: Appl. Phys.* **2007**, *40*, 4896-4901.

(18) Lim, B. S.; Rahtu, A.; Park, J.-S.; Gordon, R. G. Synthesis and Characterization of Volatile, Thermally Stable, Reactive Transition Metal Amidinates. *Inorg. Chem.* **2003**, *42*, 7951-7958.

(19) Bandoli, G.; Barreca, D.; Gasparotto, A.; Maccato, C.; Seraglia, R.; Tondello, E.; Devi, A.; Fischer, R. A.; Winter, M. A Cobalt(II) Hexafluoroacetylacetonate Ethylenediamine Complex as a CVD Molecular Source of Cobalt Oxide Nanostructures. *Inorg. Chem.* **2009**, *48*, 82-89.

(20) Dhar, S.; Varade, A.; Shivashankar, S. A. Thermodynamic Modeling to Analyse Composition of Carbonaceous Coatings of MnO and other Oxides of Manganese Grown by MOCVD. *Bull. Mater. Sci.* **2011**, *34*, 11-18.

(21) Sun, H.; Qin, X.; Zaera, F. Activation of Metal–Organic Precursors by Electron Bombardment in the Gas Phase for Enhanced Deposition of Solid Films. *J. Phys. Chem. Lett.* **2012**, *3*, 2523-2527.

(22) McElwee-White, L. Design of Precursors for the CVD of Inorganic Thin Films. *Dalton Trans.* **2006**, 5327-5333.

(23) Lee, Y.; Sun, H.; Young, M. J.; George, S. M. Atomic Layer Deposition of Metal Fluorides Using HF–Pyridine as the Fluorine Precursor. *Chem. Mater.* **2016**, *28*, 2022-2032.

J. Phys. Chem. C, **2018**, *122*, 1367–1375

DOI: 10.1021/acs.jpcc.7b10277

(24) Kurokawa, A.; Sutou, Y.; Koike, J.; Hamada, T.; Matsumoto, K.; Nagai, H.; Maekawa, K.; Kanato, H. Simultaneous Formation of a Metallic Mn Layer and a MnOx /MnSixOy Barrier Layer by Chemical Vapor Deposition at 250 °C. *Jpn. J. Appl. Phys.* **2013**, *52*, 05FA02.

(25) Mai Phuong, N.; Neishi, K.; Sutou, Y.; Koike, J. Effects of Adsorbed Moisture in SiO_2 Substrates on the Formation of a Mn Oxide Layer by Chemical Vapor Deposition. *J. Phys. Chem. C* **2011**, *115*, 16731-16736.

(26) Phuong, N. M.; Sutou, Y.; Koike, J. Structural Characterization of a Manganese Oxide Barrier Layer Formed by Chemical Vapor Deposition for Advanced Interconnects Application on SiOC Dielectric Substrates. *J. Phys. Chem. C* **2013**, *117*, 160-164.

(27) Jourdan, N.; Krishtab, M. B.; Baklanov, M. R.; Meersschaut, J.; Wilson, C. J.; Ablett, J. M.; Fonda, E.; Zhao, L.; Van Elshocht, S.; Tökei, Z.; Vancoille, E. Study of Chemical Vapor Deposition of Manganese on Porous SiCOH Low-k Dielectrics Using Bis(ethylcyclopentadienyl)manganese. *Electrochem. Solid State Lett.* **2012**, *15*, H176-H178.

(28) Dixit, V. K.; Neishi, K.; Akao, N.; Koike, J. Structural and Electronic Properties of a Mn Oxide Diffusion Barrier Layer Formed by Chemical Vapor Deposition. *IEEE Trans. Device Mater. Reliab.* **2011**, *11*, 295-302.

(29) Young, M. J.; Schnabel, H. D.; Holder, A. M.; George, S. M.; Musgrave, C. B. Band Diagram and Rate Analysis of Thin Film Spinel $LiMn_2O_4$ Formed by Electrochemical Conversion of ALD-Grown MnO. *Adv. Funct. Mater.* **2016**, *26*, 7895-7907.

(30) Nakamura, T. Intermolecular Interaction between Rare Earth and Manganese Precursors in Metalorganic Chemical Vapor Deposition of Perovskite Manganite Films. *Phys. Status Solidi C* **2015**, *12*, 958-963.

(31) Troyanov, S. I.; Gorbenko, O. Y.; Bosak, A. A. Synthesis, Crystal Structure and Properties of Manganese(II) Hexafluoroacetylacetonates $Mn(hfa)_2(H_2O)_2$ and $KMn(hfa)_3$. *Polyhedron* **1999**, *18*, 3505-3509.

(32) Lipani, Z.; Catalano, M. R.; Rossi, P.; Paoli, P.; Malandrino, G. A Novel Manganese(II) MOCVD Precursor: Synthesis, Characterization, and Mass Transport Properties of $Mn(hfa)_2$•tmeda. *Chem. Vap. Deposition* **2013**, *19*, 22-28.

(33) Carraro, G.; Maccato, C.; Gasparotto, A.; Barreca, D.; Walter, M.; Mayrhofer, L.; Moseler, M.; Venzo, A.; Seraglia, R.; Marega, C. An Old Workhorse for New Applications: $Fe(dpm)_3$ as a Precursor for Low-Temperature PECVD of Iron(III) Oxide. *Phys. Chem. Chem. Phys.* **2015**, *17*, 11174-11181.

(34) Gasparotto, A.; Barreca, D.; Bekermann, D.; Devi, A.; Fischer, R. A.; Maccato, C.; Tondello, E. Plasma Processing of Nanomaterials: Emerging Technologies for Sensing and Energy Applications. *J. Nanosci. Nanotechnol.* **2011**, *11*, 8206-8213.

(35) Zheng, J.; Yang, R.; Xie, L.; Qu, J.; Liu, Y.; Li, X. Plasma-Assisted Approaches in Inorganic Nanostructure Fabrication. *Adv. Mater.* **2010**, *22*, 1451-1473.

(36) Merritt, A. R.; Rajagopalan, R.; Carter, J. D. Synthesis of Electro-Active Manganese Oxide Thin Films by Plasma Enhanced Chemical Vapor Deposition. *Thin Solid Films* **2014**, *556*, 28-34.

(37) Maccato, C.; Bigiani, L.; Carraro, G.; Gasparotto, A.; Seraglia, R.; Kim, J.; Devi, A.; Tabacchi, G.; Fois, E.; Pace, G.; Noto, V. D.; Barreca, D. *Chem. Eur. J.* **2017**, *23*, 17954–17963. DOI: 10.1002/chem.201703423.

(38) Bandoli, G.; Barreca, D.; Gasparotto, A.; Seraglia, R.; Tondello, E.; Devi, A.; Fischer, R. A.; Winter, M.; Fois, E.; Gamba, A.; Tabacchi, G. An Integrated Experimental and Theoretical Investigation on $Cu(hfa)_2TMEDA$: Structure, Bonding and Reactivity. *Phys. Chem. Chem. Phys.* **2009**, *11*, 5998-6007.

(39) Barreca, D.; Carraro, G.; Devi, A.; Fois, E.; Gasparotto, A.; Seraglia, R.; Maccato, C.; Sada, C.; Tabacchi, G.; Tondello, E.; Venzo, A.; Winter, M. β-Fe_2O_3 Nanomaterials from an Iron(ii) Diketonate-Diamine Complex: a Study from Molecular Precursor to Growth Process. *Dalton Trans.* **2012**, *41*, 149-155.

(40) McCormack, W. B.; Sandy, C. A. *UK Patent GB 2022088A* **1979**.

(41) Frisch, M. J.; Trucks, G. W.; Schlegel, H. B.; Scuseria, G. E.; Robb, M. A.; Cheeseman, J. R.; Montgomery Jr., J. A.; Vreven, T.; Kudin, K. N.; Burant, J. C.; Millam, J. M.; Iyengar, S. S.; Tomasi, J.; Barone, V.; Mennucci, B.; Cossi, M.; Scalmani, G.; Rega, N.; Petersson, G. A.; Nakatsuji, H.; Hada, M.; Ehara, M.; Toyota, K.; Fukuda, R.; Hasegawa, J.; Ishida, M.; Nakajima, T.; Honda, Y.; O. Kitao, N., H.; Klene, M.; Li, X.; Knox, J. E.; Hratchian, H. P.; Cross, J. B.; Bakken, V.; Adamo, C.; Jaramillo, J.; Gomperts, R.; Stratmann, R. E.; Yazyev, O.; Austin, A. J.; Cammi, R.; Pomelli, C.; Ochterski, J.; Ayala, P. Y.; Morokuma, K.; Voth, G. A.; Salvador, P.; Dannenberg, J. J.; Zakrzewski, V. G.; Dapprich, S.; Daniels, A. D.; Strain, M. C.; Farkas, O.; Malick, D. K.; Rabuck, A. D.; Raghavachari, K.; Foresman, J. B.; Ortiz, J. V.; Cui, Q.; Baboul, A. G.; Clifford, S.; Cioslowski, J.; Stefanov, B. B.; Liu, G.; Liashenko, A.; Piskorz, P.; Komaromi, I.;

Martin, R. L.; Fox, D. J.; Keith, T.; Al-Laham, M. A.; Peng, C. Y.; Nanayakkara, A.; Challacombe, M.; Gill, P. M. W.; Johnson, B. G.; Chen, W.; Wong, M. W.; C., G.; Pople, J. A., GAUSSIAN 09 (Revision D.02), Gaussian, Inc., Wallingford, CT. 2009.

(42) Car, R.; Parrinello, M. Unified Approach for Molecular Dynamics and Density-Functional Theory. *Phys. Rev. Lett.* **1985**, *55*, 2471-2474.

(43) CPMD code, MPI für Festkörperforschung, Stuttgart, Germany; IBM Zürich Research Laboratory, Zürich, Switzerland, 1990–2017, www.cpmd.org.

(44) Barreca, D.; Fois, E.; Gasparotto, A.; Seraglia, R.; Tondello, E.; Tabacchi, G. How Does Cu^{II} Convert into Cu^{I}? An Unexpected Ring-Mediated Single-Electron Reduction. *Chem. Eur. J.* **2011**, *17*, 10864-10870.

(45) Fois, E.; Tabacchi, G.; Barreca, D.; Gasparotto, A.; Tondello, E. "Hot" Surface Activation of Molecular Complexes: Insight from Modeling Studies. *Angew. Chem. Int. Ed.* **2010**, *49*, 1944-1948.

(46) Tabacchi, G.; Fois, E.; Barreca, D.; Gasparotto, A. CVD Precursors for Transition Metal Oxide Nanostructures: Molecular Properties, Surface Behavior and Temperature Effects. *Phys. Status Solidi A* **2014**, *211*, 251-259.

(47) Tabacchi, G.; Fois, E.; Barreca, D.; Carraro, G.; Gasparotto, A.; Maccato, C., Modeling The First Activation Stages of the $Fe(hfa)_2TMEDA$ CVD Precursor on a Heated Growth Surface. In *Advanced Processing and Manufacturing Technologies for Nanostructured and Multifunctional Materials II*, John Wiley & Sons, Inc.: 2015; pp 83-90.

(48) Grimme, S. Semiempirical GGA-type Density Functional Constructed with a Long-Range Dispersion Correction. *J. Comput. Chem.* **2006**, *27*, 1787-1799.

J. Phys. Chem. C, **2018**, *122*, 1367–1375

DOI: 10.1021/acs.jpcc.7b10277

(49) Barreca, D.; Carraro, G.; Gasparotto, A.; Maccato, C.; Sada, C.; Singh, A. P.; Mathur, S.; Mettenbörger, A.; Bontempi, E.; Depero, L. E. Columnar Fe_2O_3 Arrays via Plasma-Enhanced Growth: Interplay of Fluorine Substitution and Photoelectrochemical Properties. *Int. J. Hydrogen Energy* **2013**, *38*, 14189-14199.

(50) Briggs, D.; Seah, M. P., *Practical surface analysis: Auger and X-ray photoelectron spectroscopy*. John Wiley & Sons: New York, 2nd ed.: 1990.

(51) Barreca, D.; Carraro, G.; Gasparotto, A.; Maccato, C.; Seraglia, R.; Tabacchi, G. An iron(II) Diamine Diketonate Molecular Complex: Synthesis, Characterization and Application in the CVD of Fe_2O_3 Thin Films. *Inorg. Chim. Acta* **2012**, *380*, 161-166.

(52) Gasparotto, A.; Barreca, D.; Bekermann, D.; Devi, A.; Fischer, R. A.; Fornasiero, P.; Gombac, V.; Lebedev, O. I.; Maccato, C.; Montini, T.; Van Tendeloo, G.; Tondello, E. F-Doped Co_3O_4 Photocatalysts for Sustainable H_2 Generation from Water/Ethanol. *J. Am. Chem. Soc.* **2011**, *133*, 19362-19365.

(53) Pattern N° 024-0727, JCPDS (2000).

(54) Pattern N° 024-0735, JCPDS (2000).

(55) http://srdata.nist.gov/xps.

(56) Carraro, G.; Barreca, D.; Bekermann, D.; Montini, T.; Gasparotto, A.; Gombac, V.; Maccato, C.; Fornasiero, P. Supported F-Doped ε-Fe_2O_3 Nanomaterials: Synthesis, Characterization and Photo-Assisted H_2 Production. *J. Nanosci. Nanotechnol.* **2013**, *13*, 4962-4968.

(57) Carraro, G.; Gasparotto, A.; Maccato, C.; Bontempi, E.; Lebedev, O. I.; Turner, S.; Sada, C.; Depero, L. E.; Van Tendeloo, G.; Barreca, D. Fluorine Doped Fe_2O_3 Nanostructures by a One-Pot Plasma-Assisted Strategy. *RSC Adv.* **2013**, *3*, 23762-23768.

J. Phys. Chem. C, **2018**, *122*, 1367–1375

DOI: 10.1021/acs.jpcc.7b10277

(58) Barreca, D.; Bekermann, D.; Comini, E.; Devi, A.; Fischer, R. A.; Gasparotto, A.; Gavagnin, M.; Maccato, C.; Sada, C.; Sberveglieri, G.; Tondello, E. Plasma Enhanced-CVD of Undoped and Fluorine-Doped Co_3O_4 Nanosystems for Novel Gas Sensors. *Sens. Actuators, B* **2011**, *160*, 79-86.

(59) Mishra, S.; Daniele, S. Metal–Organic Derivatives with Fluorinated Ligands as Precursors for Inorganic Nanomaterials. *Chem. Rev.* **2015**, *115*, 8379-8448.

Table of Contents (TOC) Image

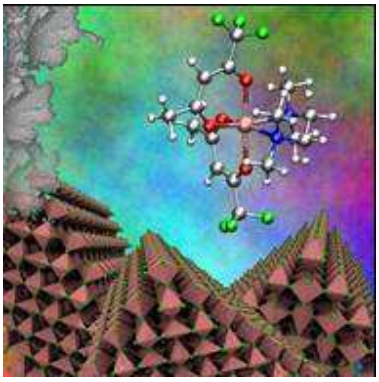

D. Barreca, G. Carraro, E. Fois, A. Gasparotto, F. Gri, R. Seraglia, M. Wilken, A. Venzo, A. Devi, G. Tabacchi, C. Maccato

Manganese(II) molecular sources for plasma-assisted CVD of Mn oxides and fluorides: from precursors to growth process